

# Mass and momentum transport from a sphere in steady and oscillatory flows

H. M. Blackburn<sup>a)</sup>

*CSIRO Manufacturing and Infrastructure Technology, P.O. Box 56, Highett 3190, Australia*

(Received 8 May 2002; accepted 5 August 2002; published 3 October 2002)

Heat or mass transfer from spherical particles in oscillatory flow has important applications in combustion and spray drying. This work provides a parametric investigation of drag forces experienced by, and transport of a passive scalar from, an isolated rigid fixed sphere in steady and oscillatory axisymmetric flows. At Schmidt (Prandtl) number of 1, oscillatory flows with Reynolds numbers in the range 1–100 and oscillation amplitudes in the range 0.05–5 sphere diameters are investigated using numerical simulation. Scalar concentration is uniform on the surface of the sphere and zero in the far field. Coefficients of peak drag for steady and oscillatory flows are presented and compared to values obtained from Basset's analytical solution for Stokes flow, and the relative contributions of the added mass, Stokes drag, and Basset history terms are examined. At the higher Reynolds numbers and amplitudes, it is found that the time-average mass transfer rate can be more than double that for diffusion in quiescent fluid, or in Stokes flow. Time-average Sherwood (Nusselt) numbers for oscillatory flows asymptote to the Stokes limit at low oscillation amplitude, regardless of Reynolds number. An unexpected result is that at intermediate Reynolds numbers and oscillation amplitudes, it is possible to depress the time-average mass-transfer coefficient slightly below that for Stokes flow. Within the Reynolds number range considered, Sherwood–Nusselt numbers in steady flow are found to be always higher than for an oscillatory flow of the same root-mean-square (rms) velocity. © 2002 American Institute of Physics. [DOI: 10.1063/1.1510448]

## I. INTRODUCTION

Heat or mass transfer from spherical particles in oscillatory flow has important applications, for example, in combustion and spray drying. As an idealization of the situation encountered in applications, where there may be many particles in more or less close proximity, giving rise to a non-uniform far-field velocity and concentration of scalar, in this work we will consider scalar transport from a single isolated sphere in a background flow with rectilinear oscillation. The scalar value is assumed to be uniform and steady on the surface of the sphere, and zero in the far-field.

Scalar and momentum transport are two aspects to this problem that are rarely dealt with together, perhaps in part because of the largely experimental basis of previous work in the area. A number of investigations of both steady and oscillatory flows past spheres at low to moderate Reynolds numbers, exist<sup>1–8</sup> but these have dealt with fluid dynamical aspects, without considering scalar transport. Even so, no systematic parametric studies that document force coefficients for spheres in oscillatory flows at moderate Reynolds numbers and amplitudes have appeared. Studies dealing in detail with scalar transport are largely confined to steady flow.<sup>9–12</sup> Analytical results have been developed for transient scalar transport from spheres at low Peclet numbers,<sup>13,14</sup> and a numerical study at finite Reynolds and Peclet numbers, dealing with a step change in scalar value, has also appeared.<sup>15</sup>

While there is technological interest in heat and mass

transfer from spheres in oscillatory flow,<sup>16</sup> often for comparatively low Reynolds and Schmidt (Prandtl) numbers, most of the published investigations have been based in physical experiment (see a review<sup>17</sup> of work up to 1976), and as such have typically dealt with Reynolds numbers above the onset of wake transition, and comparatively high Schmidt numbers. A single preliminary numerical study of scalar transport in low to moderate Reynolds number oscillatory flow past a sphere has appeared.<sup>18</sup> Those results indicate an unexpected, apparently unbounded, increase in time-average scalar transport as oscillation amplitudes are reduced to low values for all Reynolds numbers considered. A fundamental expectation is that at finite Reynolds numbers, flows will approach oscillatory Stokes flow as oscillation amplitudes approach zero. A corresponding expectation for scalar transport is that it uncouples from the flow field and asymptotes to the “Stokes flow limit,” i.e., the same uniform radial diffusion found in quiescent fluid. These expectations are confirmed by the analytical results.<sup>13,14,19</sup>

Two dimensionless groups are required to uniquely identify the oscillatory flow past a sphere; here they are chosen as the Reynolds number  $Re = U_{\max}D/\nu$  and the amplitude ratio  $A/D$ , where  $U_{\max}$  is the maximum freestream flow speed,  $D$  is the sphere diameter,  $\nu$  is the fluid kinematic viscosity and  $A$  is the amplitude of freestream fluid particle motion. In oscillatory flows,  $U_{\max} = \omega A$ , in which  $\omega$  is the angular frequency of oscillation, while in the steady flows also considered here,  $U_{\max}$  is taken as the freestream speed. The Reynolds number and amplitude ratio are sometimes combined in a Stokes number,  $St = \omega D^2/\nu = Re/(A/D)$ .

The passive scalar can be thought of either as tempera-

<sup>a)</sup>Electronic mail: hugh.blackburn@csiro.au

ture or mass concentration; the two can be considered equivalent at the same numerical values of Prandtl and Schmidt ( $Sc$ ) number, owing to the analogous behavior of heat and mass transfer. The remainder of the discussion will be couched in terms of Schmidt and Sherwood ( $Sh$ ) numbers for mass diffusivity and transport coefficient, respectively, with the understanding that these are interchangeable with Prandtl and Nusselt numbers.

The current study comprises a numerical investigation of scalar and momentum transport from a sphere in both steady and oscillatory incompressible flows in the range of Reynolds numbers  $1 \leq Re \leq 100$ . Flow oscillation amplitudes fall in the range  $0.05 \leq A/D \leq 5$ . The Schmidt number here is taken to be unity, a value that is broadly representative of mass diffusion from liquid droplets in gases,<sup>20</sup> so the values of Sherwood numbers computed, and behavioral trends, can be also considered typical for this application. In addition, as the value is relatively close to the Prandtl number for air, the results and trends will be approximately correct for heat transfer from spheres in air flows.

In steady uniform flow, sphere wakes are steady and axisymmetric at Reynolds numbers up to  $Re_{c1} \approx 210$ , where a supercritical bifurcation to nonaxisymmetric, but still steady, flow occurs.<sup>3,4,7</sup> Subsequently, a supercritical Hopf bifurcation to oscillatory wake flow occurs at  $Re_{c2} \approx 273$ .<sup>7</sup> As the maximum Reynolds number for both steady and oscillatory flow in the current study was  $Re = 100$ , and oscillation amplitudes restricted to less than five sphere diameters, it has been assumed that the oscillatory flow retains axisymmetry. Floquet analysis will be required in order to help resolve this issue.

## II. NUMERICAL METHOD

### A. Continuum equations

The continuum equations for unsteady diffusion in an unsteady incompressible flow are

$$\partial_t \mathbf{u} + N(\mathbf{u}) = -\frac{1}{\rho} \nabla p + \nu \nabla^2 \mathbf{u}, \quad \text{with } \nabla \cdot \mathbf{u} = 0, \quad (1)$$

$$\partial_t c + C(\mathbf{u}, c) = \alpha \nabla^2 c, \quad (2)$$

where  $\mathbf{u}$  is fluid velocity and  $c$  is scalar concentration,  $p$ ,  $\rho$ , and  $\nu$ , respectively, the fluid's pressure, density, and kinematic viscosity,  $\alpha = \nu / Sc$  the scalar diffusivity. In the case that the scalar is temperature, the effect of dissipation of kinetic energy on scalar transport is assumed to be negligible. The nonlinear and convective terms  $N(\mathbf{u})$  and  $C(\mathbf{u}, c)$  can be composed in a number of ways (which are equivalent for continua); here "skew-symmetric" forms are employed, i.e.,  $N(\mathbf{u}) = (\mathbf{u} \cdot \nabla \mathbf{u} + \nabla \cdot \mathbf{u} \mathbf{u})/2$ ,  $C(\mathbf{u}, c) = (\mathbf{u} \cdot \nabla c + \nabla \cdot \mathbf{u} c)/2$ . In the present application, (1) and (2) are solved in a cylindrical coordinate system where the  $x$  coordinate is aligned with and the  $r$  coordinate is normal to the axial direction. Far-field flows are parallel to the coordinate system axis.

### B. Derived coefficients

Drag coefficients are computed using the peak free-stream flow speed

$$C_d = \frac{8F_d}{\rho U_{\max}^2 \pi D^2}, \quad (3)$$

the drag force is exerted by pressure and viscous traction

$$F_d = 2\pi \int \mathbf{e}_1 \cdot \{n p - \mu \mathbf{n} \cdot [\nabla \mathbf{u} + (\nabla \mathbf{u})^T]\} r ds, \quad (4)$$

where  $\mathbf{n}$  is the domain unit outward normal,  $\mathbf{e}_1$  is the unit axial vector and the integral is taken around the perimeter of the sphere outline in the meridional semiplane of the cylindrical coordinate system. The Sherwood number is computed as<sup>19</sup>

$$Sh = \frac{2}{D^2(c_{\max} - c_{\infty})} \int \mathbf{n} \cdot \nabla c r ds. \quad (5)$$

Time-mean values, such as  $\overline{Sh}$ , are cycle-average values, while (cyclic) peak values are indicated as  $\widehat{C}_d$ . Both time-mean and peak values were computed from cubic spline interpolations of time series data.

### C. Time integration

The Navier–Stokes and scalar transport equations (1) and (2) are integrated in time using a mixed explicit–implicit time-splitting scheme based on backwards differentiation.<sup>21</sup> The original scheme was designed to integrate the momentum equations (1) alone; changes have been made as required to incorporate scalar transport: scalar convection is handled explicitly while diffusion is handled implicitly. A second-order-time variant of the method was employed for all calculations.

### D. Spatial discretization

An axisymmetric cylindrical-geometry spectral element method was employed for spatial discretization. Expansion functions within each element are tensor products of Lagrange polynomials that use the Gauss–Lobatto–Legendre (GLL) points as knots. The adaption of the standard spectral element method to a cylindrical coordinate system has some similarities to previous formulations.<sup>4,5</sup> Helmholtz problems that arise in the time-split are symmetrized by pre-multiplication by  $r$ , while any remaining singular terms on the axis are set to zero. This approach has been shown to preserve exponential convergence for axisymmetric Stokes problems.<sup>22,23</sup> An extension of the method has been made to nonaxisymmetric flows.<sup>24</sup>

Where integral quantities such as drag forces and surface fluxes are required, e.g., in (4) and (5), these were computed using Gauss–Lobatto quadrature. Azimuthal vorticity was computed from the velocity field via collocation differentiation during post-processing.

Mesh design for the present application in oscillatory flows is a compromise between the extremely fine radial resolution required near the sphere, particularly for low oscillation amplitudes and high Reynolds numbers, and a large domain size required for flows and scalar transport approaching the Stokes limit. The spectral element mesh adopted for the results presented here meets both these requirements, as Fig. 1 illustrates. The domain-size extents of this mesh are  $x_{\max}/D = \pm 50$ ,  $r_{\max}/D = 50$ , and the layer of elements nearest

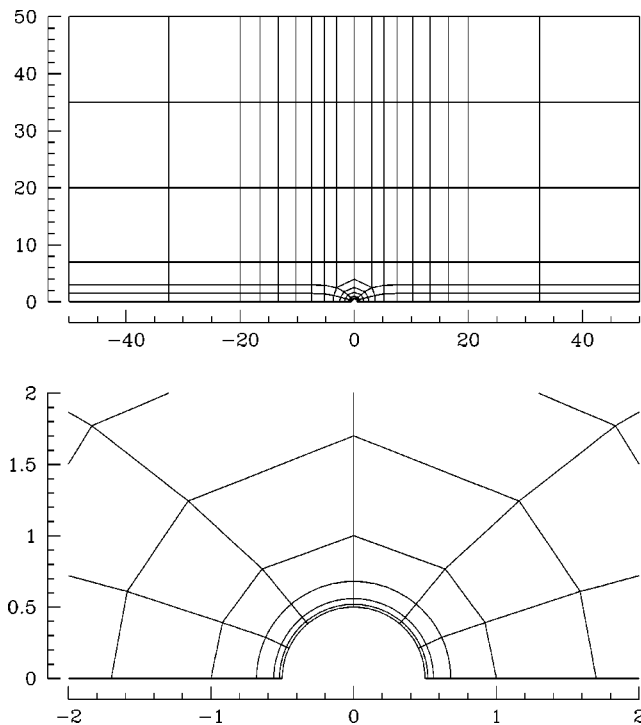


FIG. 1. Spectral element mesh, upper: full mesh, 146 elements; lower: detail, close to sphere. Dimensions are given in terms of sphere diameter  $D$ ; the inner-most layer of elements is  $0.02 D$  thick.

the sphere wall is  $0.02 D$  thick in the wall-normal direction. Other meshes of smaller extent ( $x_{\max}/D = \pm 20$ ,  $r_{\max}/D = 20$ ) and lesser near-wall refinement have also been employed during testing and check runs.

**E. Boundary conditions**

At solid walls, no-slip boundary conditions are applied to velocity variables, and a nonzero scalar concentration  $c_{\max}$  is prescribed. In the case of oscillatory flow, time-varying velocities and zero scalar concentration are prescribed at far-field boundaries. For steady flow, a constant velocity and zero scalar value are set on far-field boundaries except the outflow boundary, where zero normal gradients of velocity and scalar variables are applied, and the pressure is set to zero. For all boundaries other than the steady-flow outflow, a “high-order” pressure boundary condition<sup>21</sup> is obtained by taking the dot product of the domain unit outward normal with the momentum equations to produce

$$\partial_n p = \rho \mathbf{n} \cdot (-N(\mathbf{u}) - \nu \nabla \times \nabla \times \mathbf{u} - \partial_t \mathbf{u}), \tag{6}$$

where the rotational form of the viscous term exploits the solenoidality of the velocity. This formulation allows the time-split to retain the same accuracy as the differencing scheme used to integrate  $\partial_t \mathbf{u}$ . On the axis, the appropriate boundary conditions are  $\partial_n u = v = \partial_n c = \partial_n p = 0$ , where  $u$  is the axial and  $v$  the radial velocity component.

It should be noted that the far-field boundary condition for scalar concentration in the Stokes flow limit is

$$c_\infty = c_{\max} D / 2(x^2 + r^2)^{1/2}. \tag{7}$$

This would be a valid approximation at low Reynolds numbers and oscillation amplitudes, but as most interest is at the

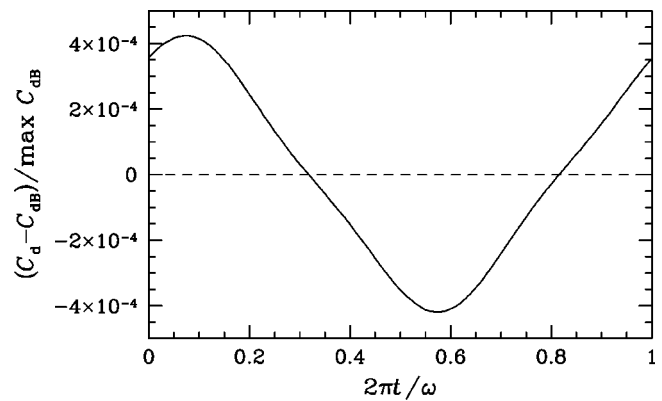


FIG. 2. Relative difference between the computed time variation of coefficient of drag force acting on a sphere in oscillatory flow at  $Re = 1$ ,  $A/D = 0.05$  and that given by Basset’s analytical solution for unsteady Stokes flow.

higher Reynolds numbers, it was decided to use  $c_\infty = 0$  at the far-field boundary for all flows, and employ a large domain size in order to compensate. It can be assumed that the maximum error in the scalar transport results presented here is dominated by this assumption: (7) provides a representative value of 1%, based on the domain size employed (see also Fig. 3). Also, the largest errors can be assumed to occur at the lower Reynolds numbers.

**F. Verification and resolution studies**

In order to verify the performance of the computational method in oscillatory flow, we first compare the time variation of drag coefficient at ( $Re = 1$ ,  $A/D = 0.05$ ) with Basset’s analytic solution for drag force in unsteady Stokes flow.<sup>2,25</sup>

$$C_{dB} = -\frac{4}{3A/D} \sin \omega t - \frac{2}{3A/D} \sin \omega t + \frac{24}{Re} \cos \omega t - \frac{12}{(Re A/D)^{1/2}} \sin(\omega t - \pi/4), \tag{8}$$

is the asymptotic unsteady coefficient of drag predicted by Basset’s solution for a sphere immersed in flow with freestream (axial) velocity  $U = \omega A \cos \omega t$ . The four contributions to the total drag in (8) result from:

- (1) The pressure gradient required to accelerate the fluid in the free-stream—if instead, the sphere is made to oscillate in quiescent fluid, this term is zero;
- (2) the force required to accelerate the volume of fluid displaced by passage of the sphere: This is the “added mass” term;
- (3) Stokes drag, the only term that does not disappear in steady motion;
- (4) forces due to the cumulative effect of vorticity diffused from the surface of the sphere in its past motion—this is the “Basset history” term, and more precisely stated it is only this term that is due to Basset.

The relative difference between the numerical Navier–Stokes solution and Basset’s Stokes solution is shown in Fig. 2. The maximum relative difference is approximately  $4 \times 10^{-4}$  and has an approximately sinusoidal variation in

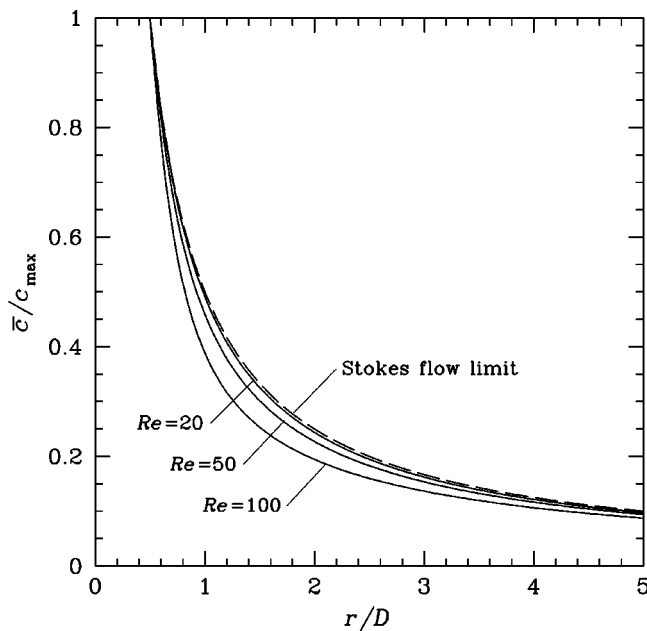


FIG. 3. Profiles of time-average scalar concentration obtained on the  $x=0$  traverse for  $A/D=0.05$ . The profiles asymptote towards the Stokes flow limit as Reynolds number is decreased. Profiles for  $Re \leq 20$  are visually indistinguishable. The slight systematic deviation from the exact Stokes flow limit is caused by the use of the far-field boundary condition  $c_\infty=0$  as opposed to the Stokes value  $c_{\max}/2(x^2+r^2)^{1/2}$ —see Sec. II E.

time, although the third harmonic makes a significant contribution. The maximum value is nearly identical to that computed in an earlier study<sup>2</sup> at a lower Reynolds number but the same oscillation amplitude ( $Re=0.1$ ,  $A/D=0.05$ ).

At low oscillation amplitudes, the scalar transport asymptotes to the Stokes flow limit (i.e., uniform radial diffusion) as Reynolds numbers approach zero.<sup>14</sup> This effect is observed in Fig. 3, which shows profiles of  $\bar{c}$  along the line  $x=0$  for  $A/D=0.05$ : at the lowest Reynolds numbers, the profiles asymptote towards the Stokes flow limit (but see the remarks in Sec. II E concerning the effects of boundary conditions on errors).

Additional evidence of the correct operation of the computational method is given by the good agreement with results previously obtained in steady flows, as discussed in Sec. III.

Mesh resolution studies have been carried out at each limit of the  $(Re, A/D)$  control space for which oscillatory flow results are presented. Only those for  $Re=100$ ,  $A/D=0.05$  are given here, in Table I, as they demonstrated the greatest variation with GLL shape function order,  $N_p$ . The results were collected after sufficient number of flow oscillations had taken place for the flow to reach an asymptotic state. This was especially important at the  $(Re=100, A/D=0.05)$  combination, where over 10 000 oscillation cycles were required for the reported scalar transport results to become asymptotic to within five significant figures. All reported oscillatory flow results are for a time step that is 1/1000th of an oscillation period, i.e.,  $\Delta t=0.002\pi/\omega$ .

Subsequent to the resolution studies, a GLL polynomial order  $N_p=4$  was selected to obtain the results of parametric investigations of oscillatory flow to be presented in Sec. IV,

TABLE I. Results of spectral element order convergence tests conducted at  $Re=100$ ,  $A/D=0.05$ .  $N_p$ , GLL shape function order;  $\widehat{C}_d$ , peak coefficient of drag;  $\overline{Sh}$ , cycle-average Sherwood number;  $\hat{u}$ ,  $\hat{v}$ ,  $\hat{c}$ , peak values at  $x/D=0.65$ ,  $r/D=0.1$ .

$N_p$	$\widehat{C}_d$	$\overline{Sh}$	$\hat{u}$	$\hat{v}$	$\hat{c}$
2	43.607	2.4202	0.175 83	0.035 974	0.779 22
4	43.986	2.4796	0.174 04	0.031 867	0.768 76
6	43.983	2.4784	0.174 18	0.031 829	0.768 83
8	43.983	2.4780	0.174 18	0.031 832	0.768 87
10	43.983	2.4778	0.174 18	0.031 831	0.768 88

since all values were converged to three significant figures or better at this level. Where it was considered prudent, these computations were backed up with spot-checks using  $N_p=6$ , but no significant differences to the  $N_p=4$  solutions were detected. For the steady flow results to be presented in Sec. III,  $N_p=8$  was used, as asymptotic values could readily be obtained without significant demand on computer resource.

### III. STEADY FLOW

The same spectral element mesh as designed for oscillatory flows (Fig. 1) was used to compute the steady-flow results.

#### A. Force coefficients

Figure 4 shows coefficients of drag (total, viscous and pressure) as functions of Reynolds number over the range  $1 \leq Re \leq 100$ . Viscous drag is the dominant component until Reynolds numbers just above 100 are reached, where pressure drag is about to become dominant. In Fig. 4, lines showing values for Stokes' solution ( $C_d=24/Re$ ) and Oseen's

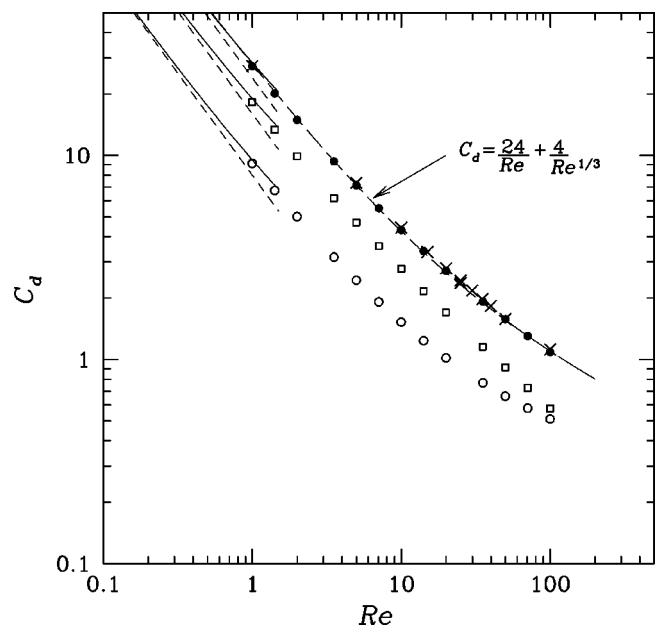


FIG. 4. Sphere drag coefficients for steady flow, as a function of Reynolds number. Total drag,  $\bullet$ ; viscous drag,  $\square$ ; pressure drag,  $\circ$ ; Stokes' solution,  $---$ ; Oseen's approximation,  $---$ ; fitted curve,  $---$ ,  $C_d=24/Re+4/Re^{1/3}$ . Independent computational results, Refs. 2 and 3.

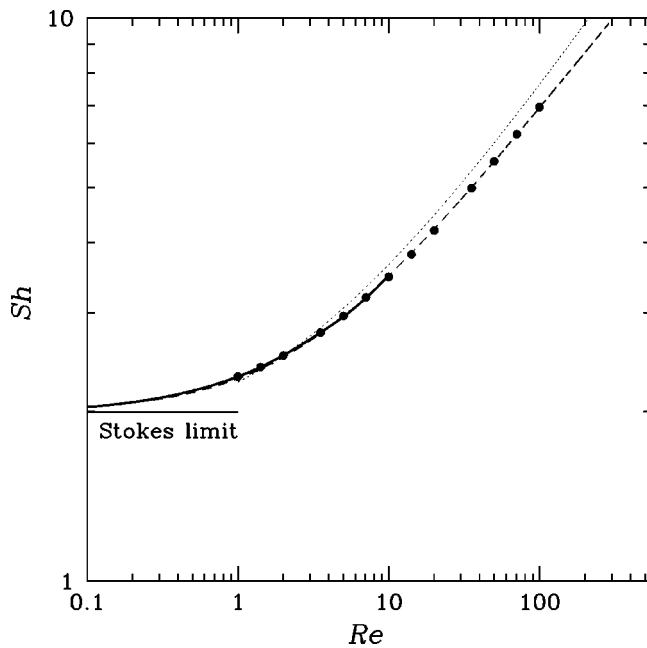


FIG. 5. Sphere Sherwood number for  $Sc = 1.0$  in steady flow, as a function of Reynolds number. Computed values, ●; asymptotic expansions (Ref. 12), —; correlation (Ref. 19) for  $1 < Re < 400$ , · · · · ·; fitted curve, - - - ( $Sh = [2^{2.693} + (1.475Re^{1/3})^{2.693}]^{1/2.693}$ ).

approximation<sup>26</sup> are also displayed, and it can be seen that the computed results asymptote to values for Oseen’s approximate solution at the lowest Reynolds numbers. A simple and accurate correlation for the total coefficient of drag, up to  $Re = 100$ , is given by

$$C_d = \frac{24}{Re} + \frac{4}{Re^{1/3}}. \tag{9}$$

For purposes of comparison, values of  $C_d$  obtained in two independent computational studies<sup>2,3</sup> are also presented in Fig. 4, and it can be seen that the present results match these well. Most of the small differences between the three sets of results can probably be attributed to somewhat smaller domain extents used in the earlier works ( $R_{max} = 25D$  used by Chang and Maxey<sup>2</sup> and  $15D$  used by Johnson and Patel<sup>3</sup> cf.  $50D$  here), with the higher blockages contributing to the slightly higher values of  $C_d$  computed in the previous studies.

**B. Mass transfer coefficients**

Figure 5 shows the Sherwood number as a function of Reynolds number. At low Reynolds numbers, the Sherwood number asymptotes to the Stokes flow limit,<sup>19,14</sup>  $Sh = 2$ , and for  $Re \leq 10$  the computed values are in excellent agreement with results obtained for  $Sc = 1$  using matched asymptotic expansions.<sup>12</sup> The computed values are in reasonable agreement with a previously published correlation [Eqs. (5)–(25), Clift, Grace, and Weber<sup>19</sup>] fitted to numerical results for a wide range of Schmidt/Prandtl numbers available up to 1975, and which for  $Re \leq 1$  (below its quoted range of applicability) agrees poorly with the analytical results.<sup>12</sup> As Reynolds numbers increase, the  $Sh-Re$  relationship asymptotes to an

approximate 1/3-power law, at least up to  $Re = 100$ , according to the results shown in Fig. 5. A blending-function approach provides the following fit:

$$Sh = [2^{2.693} + (1.475Re^{1/3})^{2.693}]^{1/2.693}. \tag{10}$$

Although originally fitted to the Stokes flow limit and present computational data only, this is seen in Fig. 5 to also match well with the analytical results<sup>12</sup> down to lower Reynolds numbers—the new correlation (10) is virtually indistinguishable from the low- $Re$  asymptotic expansion values.

**IV. OSCILLATORY FLOW**

**A. Time-dependent flows and scalar transport**

Here we examine instantaneous contours of azimuthal vorticity and scalar concentration in subsets of the computational domain for three points in the  $(Re, A/D)$  control space. In each case, the contours illustrate flows for half a motion cycle at 1/16th-period phases, starting at time  $t = 0$  in  $U = U_{max} \cos \omega t$ .

Figure 6 illustrates the flow at  $(Re = 100, A/D = 0.05)$ ; the highest Reynolds number, lowest amplitude case. Essentially all the vorticity remains in nearly spherical-shell boundary layers, extremely close to the sphere, with vorticity in each shell alternating in sign on a traverse normal to the sphere surface. The slight asymmetry of vorticity in the axial direction, most visible in Figs. 6(d)–6(f), is the key feature of the vorticity field that distinguishes this from an equivalent Stokes flow. The difference from Stokes flow is more readily apparent in the general shape of the scalar contours [Figs. 6(i)–6(p)], which besides having a small axial asymmetry, are distinctly prolate at locations remote from the sphere.

Figure 7 illustrates the flow at  $(Re = 20, A/D = 0.5)$ . The Reynolds number is smaller than for the previous case by a factor of five, which in part accounts for the larger radial length scales at which the vorticity alternates in sign on traverses outward from the surface of the sphere. Despite the reduced Reynolds number, the effects of advection of vorticity are more noticeable in Fig. 7 than they are in Fig. 6, owing to the increased oscillation amplitude. Interestingly, while there is distinct axial asymmetry in the contours of scalar concentration, the departure from shells of spherical shape (although not necessarily centered on the sphere) is greatest at radii of the order of one sphere diameter from the origin. An additional interesting feature of this case is that the time-average Sherwood number is actually depressed slightly below the Stokes flow limit, one of the small number of cases where this is so (see Sec. IV D).

The effects of advection on transport of both vorticity and scalar concentration are clearly evident at  $Re = 100, A/D = 5$ , as shown in Fig. 8. Both vorticity and scalar concentration are swept sufficiently far from the sphere in each motion cycle that contours show local maxima, remote from the surface of the sphere, that have evolved during previous cycles.

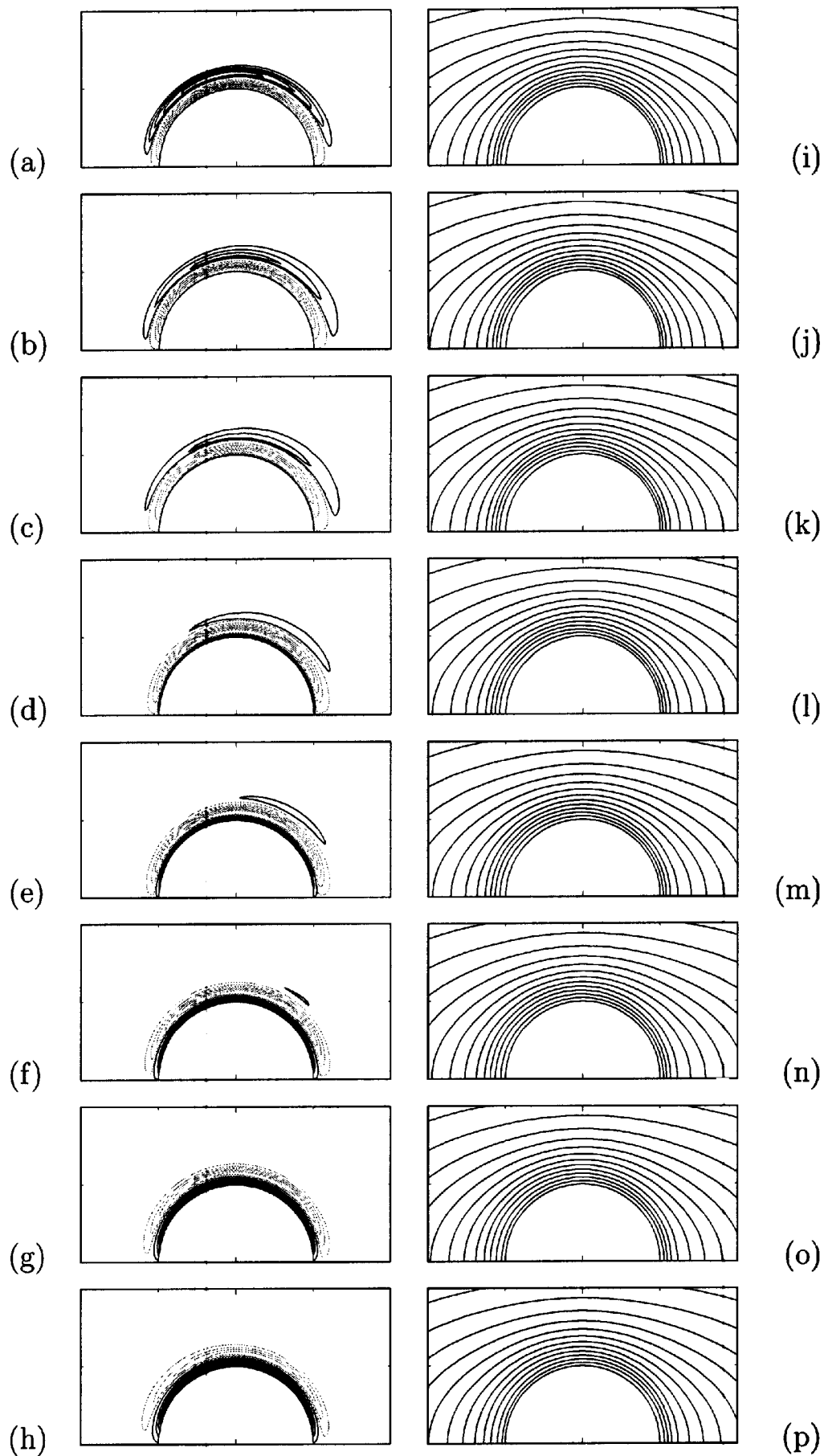


FIG. 6. Instantaneous contours of (a)–(h) positive (black) and negative (gray) azimuthal vorticity and (i)–(p) scalar concentration for ( $Re=100$ ,  $A/D=0.05$ ), shown over half a fluid motion cycle in 1/16-period phases. Fluid is initially moving to right at maximum speed. Vorticity contour increments are nonuniform to aid illustration of flow structure. Scalar contours commence at  $c_{\max}$  and continue with a uniform decrement of  $0.05 c_{\max}$ .

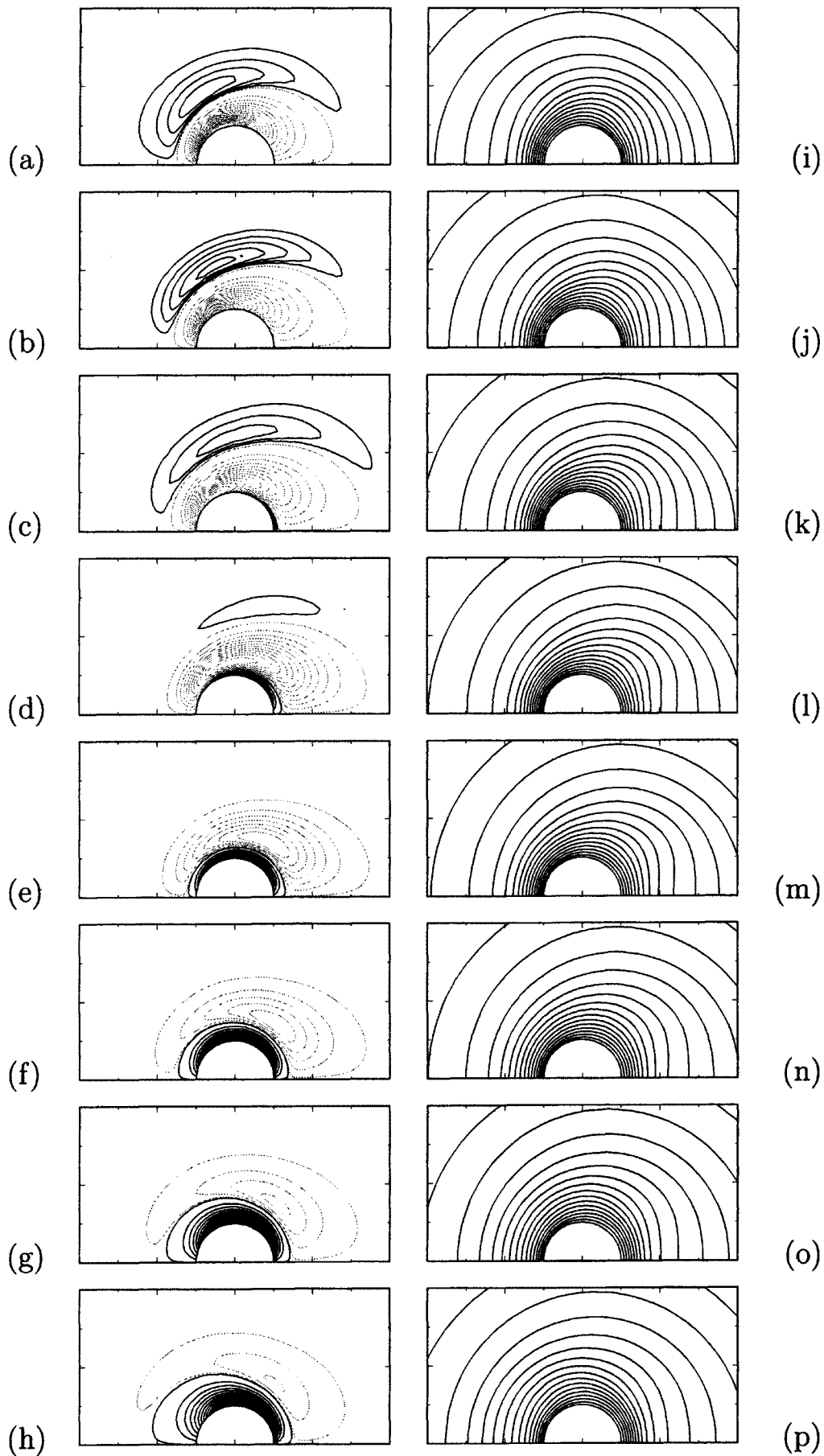


FIG. 7. Instantaneous contours of (a)–(h) positive (black) and negative (gray) azimuthal vorticity and (i)–(p) scalar concentration for  $(Re=20, A/D=0.5)$ , shown over half a fluid motion cycle in 1/16-period phases. Fluid is initially moving to right at maximum speed. Vorticity contour increments are nonuniform to aid illustration of flow structure. Scalar contours commence at  $c_{max}$  and continue with a uniform decrement of  $0.05 c_{max}$ .

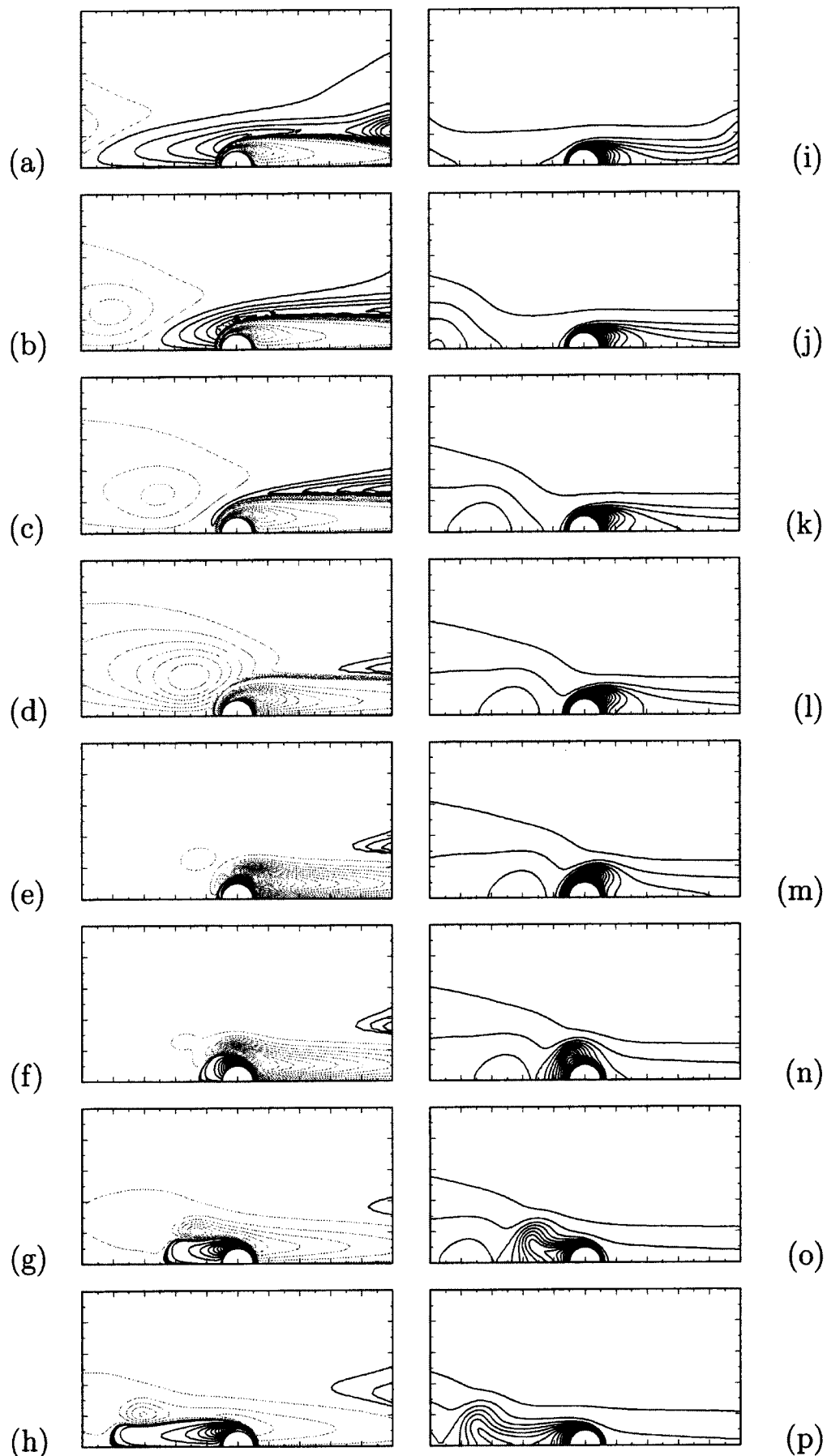


FIG. 8. Instantaneous contours of (a)–(h) positive (black) and negative (gray) azimuthal vorticity and (i)–(p) scalar concentration for ( $Re=100$ ,  $A/D=5$ ), shown over half a fluid motion cycle in 1/16-period phases. Fluid is initially moving to right at maximum speed. Vorticity contour increments are nonuniform to aid illustration of flow structure. Scalar contours commence at  $c_{\max}$  and continue with a uniform decrement of  $0.05 c_{\max}$ .

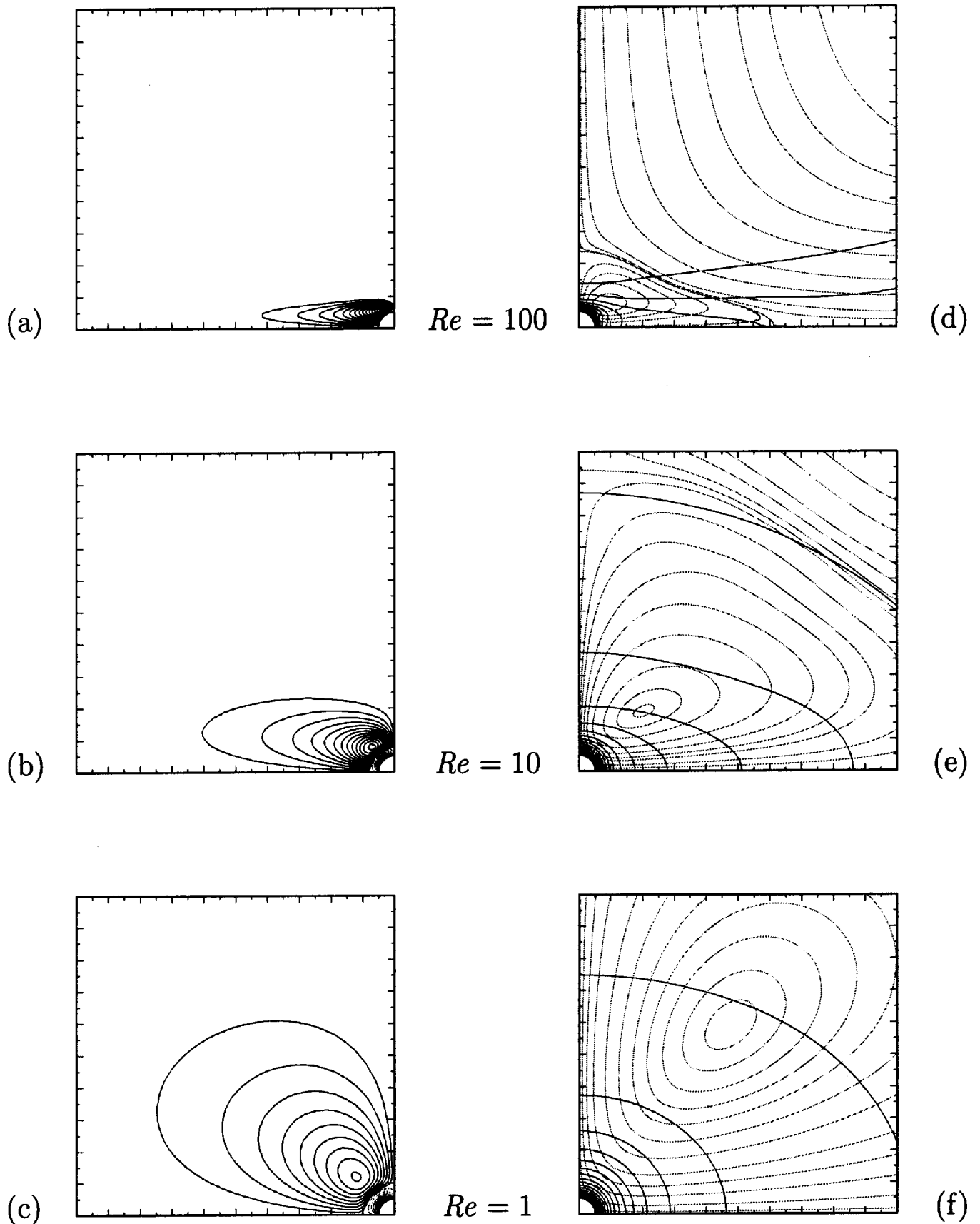


FIG. 9. Time-average vorticity, scalar concentration, and streamlines for  $A/D=5$ , Reynolds numbers as indicated: (a)–(c), contours of positive (black) and negative (gray) azimuthal vorticity; (d)–(f) contours of scalar concentration (black) overlaid with streamlines (gray). Streamline loops nearest sphere have clockwise circulations in first quadrant [i.e., in (d)–(f)]. The alignment of the free-stream oscillatory flow is horizontal.

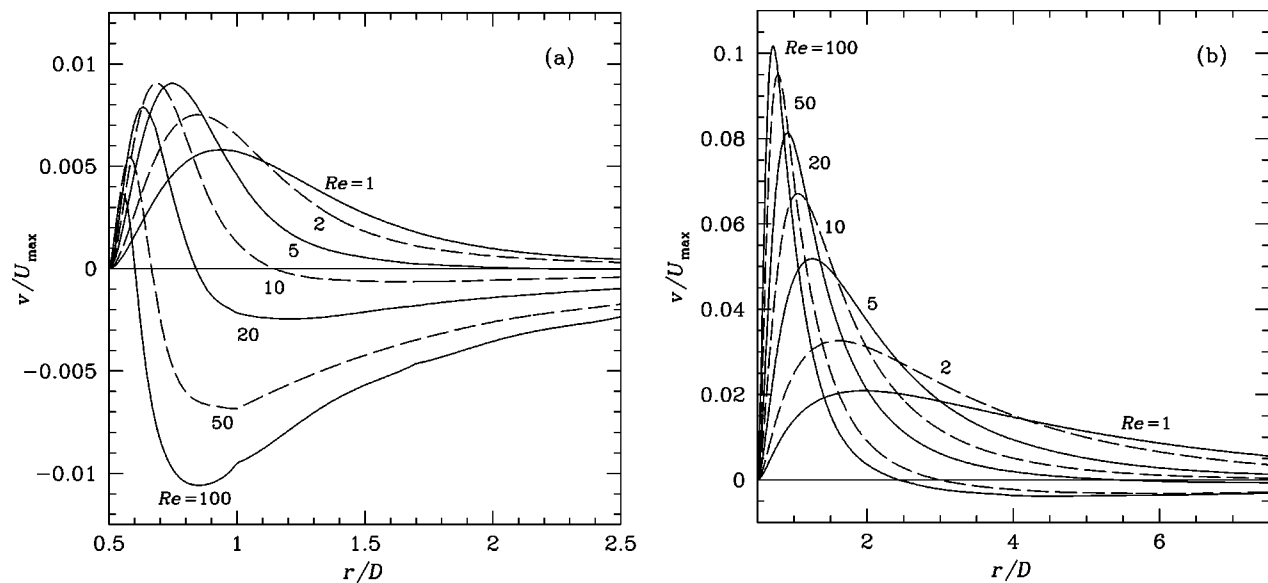


FIG. 10. Profiles of cycle-average radial velocity component  $v$  on traverses of the line  $x=0$ , for (a)  $A/D=0.05$ ; (b)  $A/D=5$ .

## B. Cycle-average flows and scalar transport

The cycle-average fluid flow displays a steady streaming component that in each quadrant of the meridional semiplane flows inward along the oscillation axis towards the stagnation point, then radially outward. Often this flow is surrounded by another circulation with opposite sense in each quadrant, however a single diagnostic parameter for existence of the second circulation cell has not yet been identified.<sup>2</sup> For oscillatory Stokes flow, only a single recirculation cell is expected in each quadrant.<sup>1</sup>

The cycle-average flows at  $A/D=5$  are illustrated for  $Re=100, 10$ , and  $1$  in Fig. 9; contours of time-average vorticity are shown in Figs. 9(a)–9(c), while contours of time-average scalar concentration are shown overlaid with time-average streamlines in Figs. 9(d)–9(f). Time-average vorticity exhibits the multilayer structure seen for the instantaneous flows (as is true for all sets of computed results), but the influence of Reynolds number on prolation of the vorticity field is clearly evident. Also, the length scale over which vorticity alternates in sign near the surface of the sphere falls as Reynolds number increases. A feature that is not obvious from the contour plots is that vorticity magnitudes fall as Reynolds number is decreased.

The time-average flow, as illustrated by the streamline patterns in Figs. 9(d)–9(f), shows that the inner region of streaming flow grows larger as Reynolds number decreases: a bounding streamline between the two circulation cells can be seen in each of Figs. 9(d) and 9(e), but not in Fig. 9(f). Not evident from the streamline patterns is that the peak streaming velocity in the inner cell increases with Reynolds number (at least at  $A/D=5$ , but this is not necessarily the case at lower amplitudes, see below). While the time-average scalar advective transport is not solely produced by the time-average flows—scalar–velocity correlations also have a role—there seems to be a clear linkage between the time-average flow and the scalar transport contours, particularly at  $Re=100$ . In that case, the inner streaming flow along the

(horizontal) flow oscillation axis towards the surface of the sphere produces an observable depression in the scalar contours on the axis (at a radius of approximately one sphere diameter). The inner flow then advects scalar first radially outwards (vertically), then axially (horizontal). As inner flow advection velocities fall, departing the immediate vicinity of the sphere, cross-flow diffusion starts to dominate, and scalar is able to cross the mean streamlines into the outer recirculation, enabling it to be transported far from the origin.

While the time-average vorticity field always displays shells of alternating sign, it is not clear if a two-celled streaming flow is always present in each quadrant. In order to examine the cell structure of streaming flow, profiles of radial velocity obtained along the line  $x=0$  (i.e., on a radial traverse, normal to the fluid oscillation axis) have been extracted at  $A/D=0.05$  and  $5$  for all Reynolds numbers studied. Details of these profiles near the sphere are shown in Fig. 10. Recirculation cell boundaries correspond to zero-crossings in these plots. Evidently, two-celled topologies exist at the highest Reynolds numbers for each of these two amplitudes, and as stated above, the peak velocity of the inner recirculation cell increases monotonically with Reynolds number at  $A/D=5$ .

To help clarify the issue of number and extent of recirculation cells, the radial locations of the first zero-crossings of radial velocity component  $v$  have been extracted from the data used to prepare Fig. 10, and plotted in Fig. 11. It appears that the size of the inner recirculation cell grows without bound as Reynolds numbers are reduced, at least until the zero-crossing location approaches the maximum radial extent of the computational domain ( $r_{\max}=50D$ ), where the analysis becomes unreliable—for this reason, data points for largest  $r/D$  have been omitted from Fig. 11.

Contours of the time-average scalar concentration at the limits of the  $(Re, A/D)$  control space considered here are shown in Fig. 12. It can be seen that at the low-Reynolds number, low-amplitude limit ( $Re=1, A/D=0.05$ ), scalar

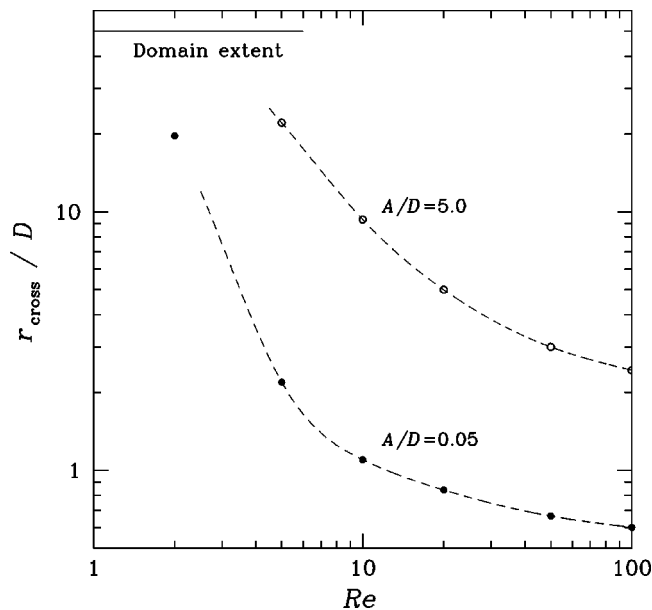


FIG. 11. Location of the first zero-crossing of the cycle-average radial velocity  $v$  on traverses of the line  $x=0$  as functions of Reynolds number, for  $A/D=0.05$  and  $A/D=5$ . Maximum radial extent of computational domain is  $r_{\max}=50D$ .

diffusion dominates, and contour lines closely approximate circular arcs, consistent with scalar transport approximating the uniform radial diffusion that represents the Stokes flow limit. At the high-Reynolds number, high-amplitude limit ( $Re=100$ ,  $A/D=5$ ), scalar advection is more significant, and the outer contours of  $c$  are clearly influenced by the time-mean streaming flow within the computational domain. In order to check domain-extent effects on sphere-surface scalar transport rates at  $Re=100$ ,  $A/D=5$ , computations were repeated on a smaller domain ( $x_{\max}/D=\pm 20$ ,  $r_{\max}/D=20$ ). While this changed the far-field contours, no significant effect on  $\overline{Sh}$  was detected.

### C. Peak force coefficients

Peak coefficients of drag in oscillatory flows are shown in Fig. 13(a). Subtracting the inertial component  $C_{d,i}=(4D/3A)\sin\omega t$ , i.e., the first term in (8), from the coefficient of drag time series prior to extracting peak values, we can also obtain the coefficient of drag for a sphere oscillating in a quiescent fluid: The corresponding peak drag coefficients are shown in Fig. 13(b). For purposes of comparison, values of peak coefficient of drag computed from Basset's analytical Stokes flow solution (8) are also plotted in Fig. 13, and it can be seen that this provides a good approximation to the total drag force up to  $A/D=1$  at the higher Reynolds numbers, and considerably above this at the lower Reynolds numbers.

In order to examine in more detail the contributions made by the various terms in Basset's solution, and how well that predicts the drag coefficients obtained computationally, the normalized drag coefficients for various combinations of terms in (8) are plotted as functions of  $Re$  at various  $A/D$  values in Fig. 14. In order to maximize the relative contributions of the Stokes drag and Basset history terms, the values

represented are for a sphere made to oscillate in quiescent fluid, i.e., the values obtained from simulation are those of Fig. 13(b), and the first term in (8) has been correspondingly omitted. For  $A/D\leq 0.2$ , peak coefficients of drag obtained from Basset's solution are virtually indistinguishable from those obtained using numerical simulation at all the Reynolds numbers employed here, and the same is true for  $A/D\leq 2$  at  $Re=1$ .

### D. Cycle-average mass transfer coefficients

Cycle-average Sherwood numbers  $\overline{Sh}$  are shown in Fig. 15 as functions of oscillation amplitude and Reynolds number. The most interesting features of this plot are associated with the high- and moderate-Reynolds number results. For  $Re=100$ , values of  $\overline{Sh}$  appear to approach a high  $A/D$  asymptote  $\overline{Sh}\approx 5$  for  $A/D\geq 2$ .  $\overline{Sh}$  falls rapidly with  $A/D$ , then recovers near  $A/D=0.2$ , before falling slowly again as  $A/D$  reaches the lowest values used in this study. For intermediate Reynolds numbers ( $Re=50, 20, 10$ ),  $\overline{Sh}-A/D$  curves have local minima for  $A/D\approx 0.3$ —in the vicinities of these minima,  $\overline{Sh}$  can fall marginally below the Stokes limit  $\overline{Sh}=2$ . For these intermediate Reynolds numbers, it seems likely that for  $A/D<0.05$ ,  $\overline{Sh}$  values will again begin to decrease, on the basis of what is observed for  $Re=100$ . For the lowest Reynolds numbers ( $Re=5, 2, 1$ ), values of  $\overline{Sh}$  asymptote monotonically to the Stokes flow limit as  $A/D$  falls. In all cases it is expected that for all Reynolds numbers the uniform  $A/D\rightarrow 0$  limit of  $\overline{Sh}$  is the Stokes flow value.

In order to gauge the mass-transfer performance in oscillatory flow relative to that in steady flow, the same values of  $\overline{Sh}$  as shown in Fig. 15(a) are repeated in Fig. 15(b), but normalized by the steady-flow values given by (10). The Reynolds number used to compute values of  $Sh_{\text{equiv}}$  from (10) is the rms value corresponding to the peak value listed in Fig. 15(a), e.g., for  $Re=100$ , the corresponding Reynolds number to compute  $Sh_{\text{equiv}}$  from (10) is  $100/2^{1/2}=70.711$ . It is immediately apparent that the normalized mass-transfer values are always less than the equivalent steady flow values. This results from pollution of the surrounding fluid with scalar effluent from previous flow cycles in the oscillatory flow case—for steady flow, there is always a continual supply of uncontaminated fluid. (The same conclusion—that the oscillatory flow values are always lower than the equivalent steady flow values—is also reached if the peak, rather than rms, Reynolds numbers are used in performing the comparison.)

## V. DISCUSSION AND CONCLUSIONS

The main results of the parametric investigations carried out in the present work are summarized in Figs. 13–15.

With regard to peak coefficients of drag in oscillatory flows (Fig. 13), an interesting finding is that Basset's analytical result for Stokes flow (8) provides a good basis for prediction of asymptotic peak drag coefficients even at quite large Reynolds numbers ( $Re\approx 100$ ), provided the oscillation amplitude is not too large ( $A/D\leq 0.5$ ). A detailed examination of the relative contributions of various terms in Basset's

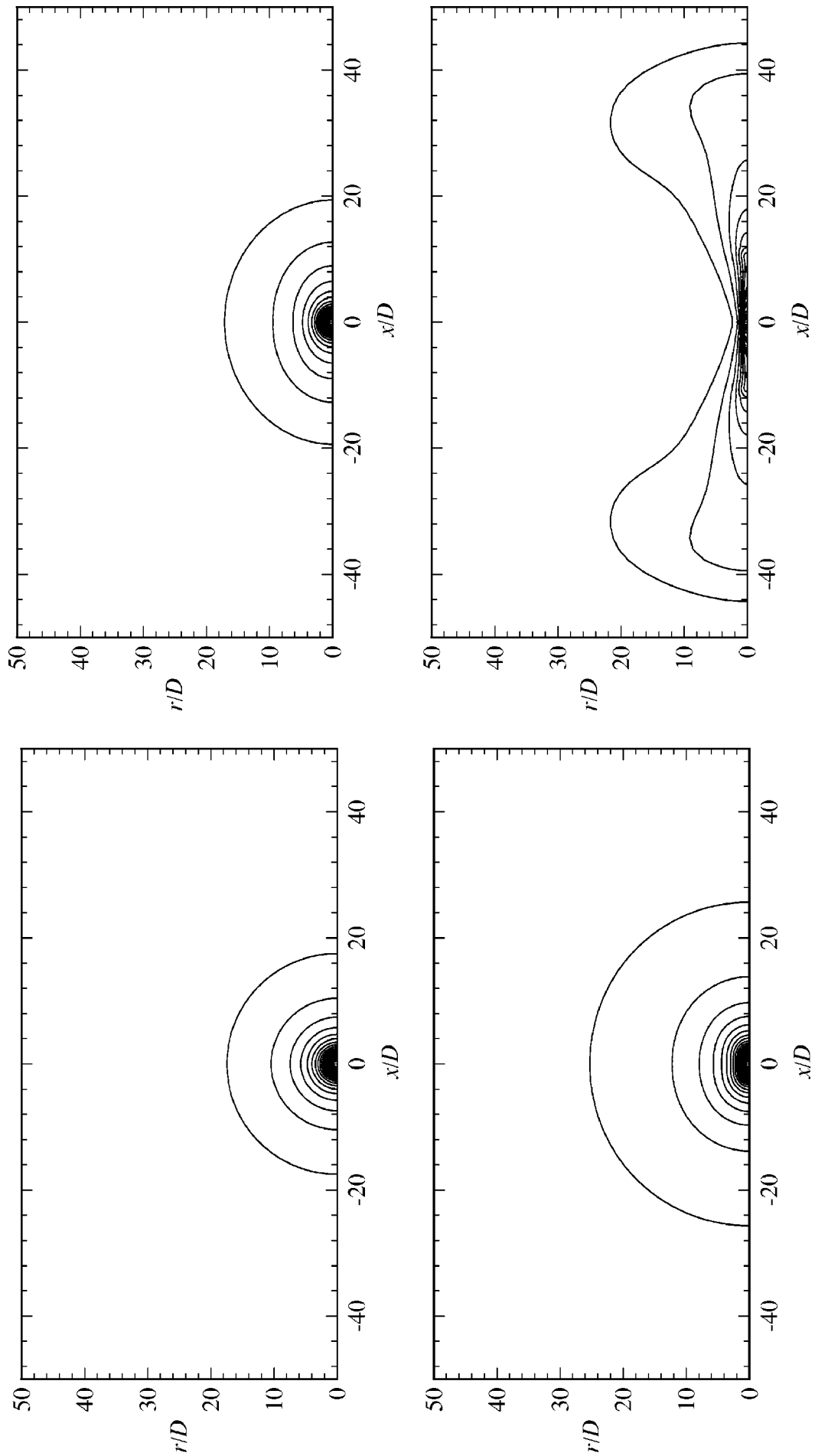


FIG. 12. Contours of time-average scalar concentration in oscillatory flows for the  $(Re, A/D)$  pairs indicated. Contour levels are identical in each case.

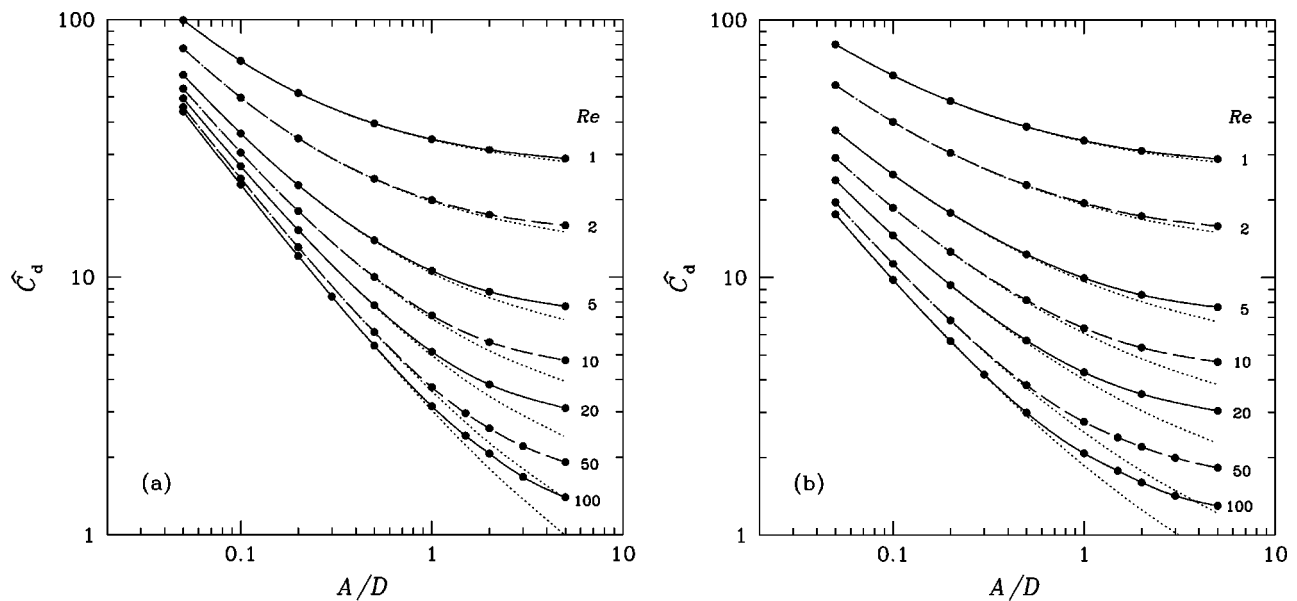


FIG. 13. Peak coefficient of drag for a sphere (a) stationary in oscillatory flow and (b) oscillating in quiescent fluid, as functions of oscillation amplitude and Reynolds number. Dotted lines ( · · · ) show predictions of Basset's solution (8) at each  $Re$ .

solution for the asymptotic drag (8), compared to the values obtained through numerical simulation (see Fig. 14) is revealing. Within the parameter ranges studied here, the contribution of the Basset history term to the total drag is always substantial, typically larger than the Stokes drag for  $A/D \leq 0.5$ . At all oscillation amplitudes, the contribution of Stokes drag becomes relatively less with increasing  $Re$ , and indeed at the lower amplitudes, the contribution of Stokes drag becomes insignificant for  $Re \geq 10$ , with added mass and history terms dominating. Again at all amplitudes, the rela-

tive contribution of the Basset history terms is greatest at intermediate values of Reynolds number (e.g., at  $Re \approx 10$  for  $A/D = 0.2$ ), and the Reynolds number at which this contribution is greatest increases with oscillation amplitude.

Time-average mass-transfer coefficients (Fig. 15) can be elevated substantially above the Stokes flow value, and within the limits of the parameter set used here, the amount of elevation appears to increase with Reynolds number. It is also possible, at least for  $Sc = 1$ , to depress time-average

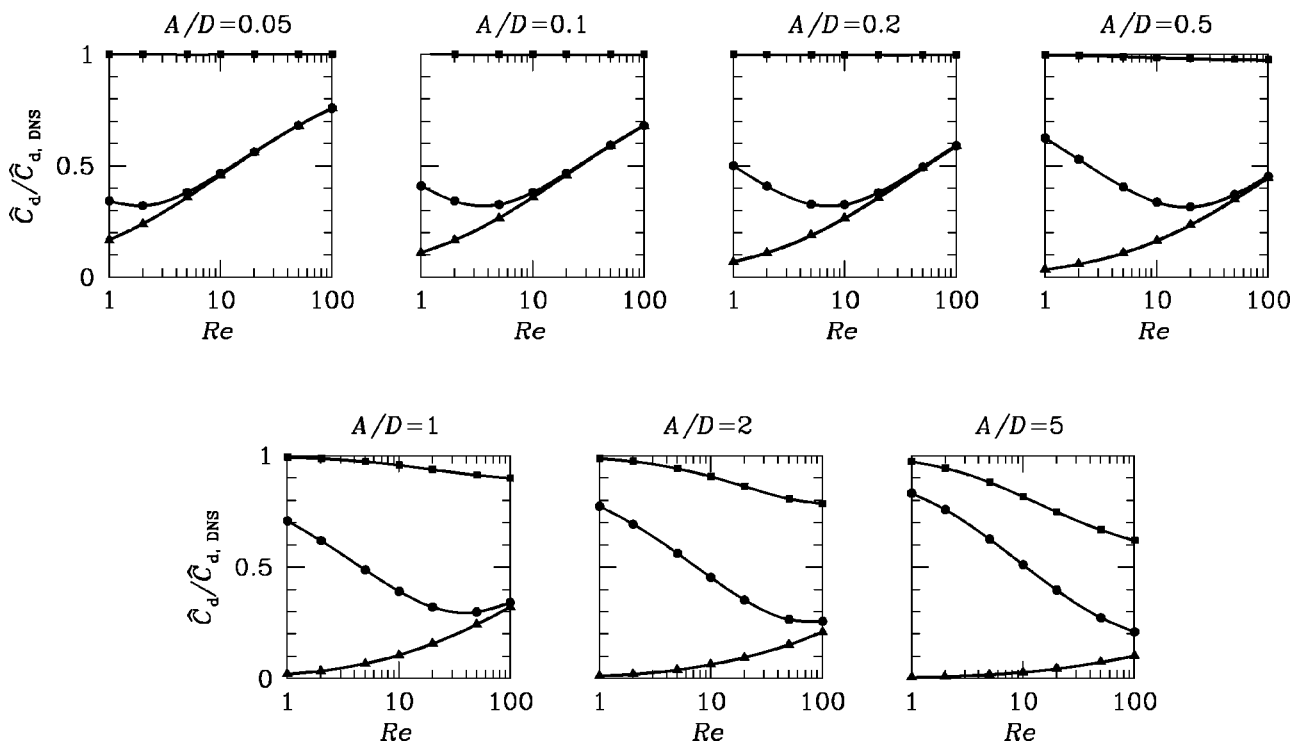


FIG. 14. Peak coefficients of drag (for a sphere oscillating in quiescent fluid) derived from Basset's solution (8), normalized by the values obtained computationally ( $\hat{C}_{d,DNS}$ ). Added mass term only,  $\blacktriangle$ ; added mass + Stokes drag,  $\bullet$ ; added mass + Stokes drag + Basset history term,  $\blacksquare$ .

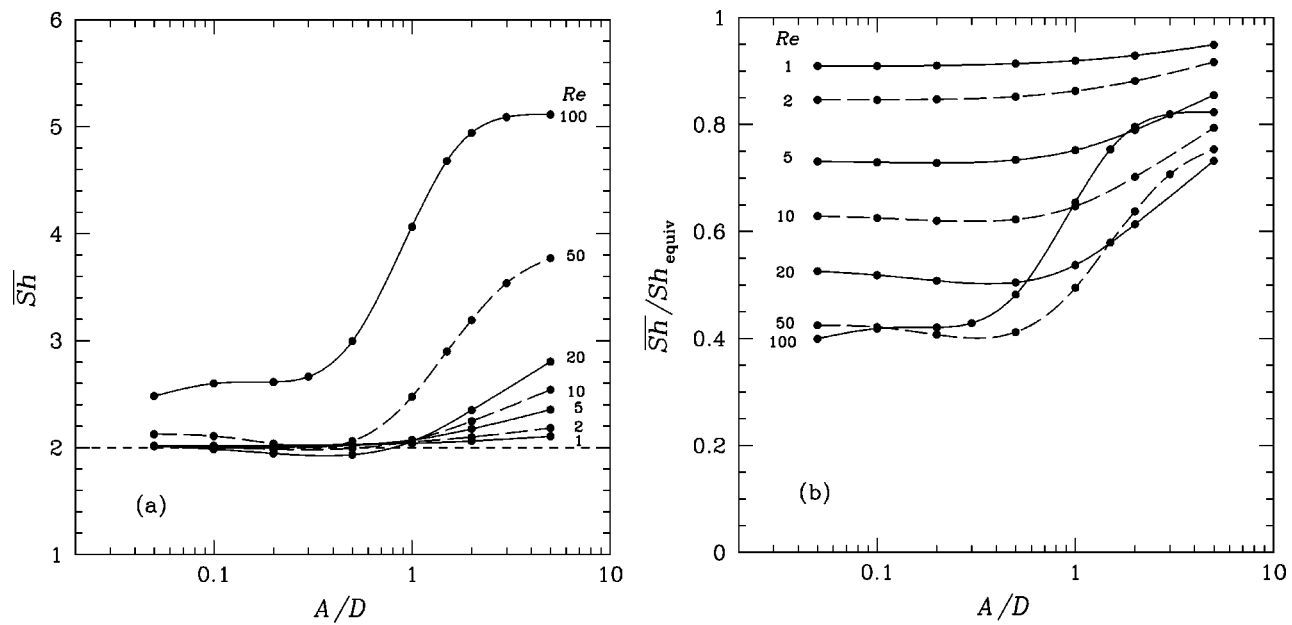


FIG. 15. (a) Cycle-average Sherwood number for  $Sc = 1.0$  in oscillatory flows, as functions of oscillation amplitude  $A/D$  and Reynolds number. Computed values,  $\bullet$ ; Stokes' flow limit,  $Sh = 2$ ,  $---$ . (b) Cycle-average Sherwood number normalized by the corresponding rms steady flow value.

mass-transfer coefficients below the Stokes flow value, although not by a large amount.

Previous computational predictions of scalar transport in oscillatory flows,<sup>18</sup> which showed  $\overline{Sh}$  climbing without bound as  $A/D \rightarrow 0$  now appear erroneous, most likely as a result of low mesh resolution near the surface of the sphere. In that work, the radial distance to the first mesh point away from the sphere wall was approximately 10% of the sphere radius, which is obviously inadequate when the flow oscillation amplitude may be of the same order, or at moderate Reynolds number, when boundary layers are thin. The correct  $A/D \rightarrow 0$  asymptotic value of  $\overline{Sh}$  is the Stokes flow limit,  $Sh = 2$ , regardless of Reynolds number or Schmidt number,<sup>14</sup> a theoretical conclusion supported by the simulation results presented here.

Time-average mass transfer coefficients in oscillatory flow were found to be lower than the corresponding rms steady-flow value. However, in potential drying applications, oscillatory flow will usually be superimposed on a background quasi-steady flow. Small droplets or particles will asymptote to a rest state with respect to the background flow, hence a more relevant basis of comparison of mass transfer

performance in these kind of flows is the Stokes flow limit. Although in most cases, mass transfer coefficients in oscillatory flows are above the Stokes flow limit value, it is also possible to obtain values somewhat below this, so that good design of drying equipment for these applications requires careful consideration.

Regarding the flow field, an issue not previously resolved in examinations of oscillatory axisymmetric flows around spheres has been the number of recirculation cells present in the time-average streaming flow.<sup>1,2</sup> While a purely numerical approach is probably not the most appropriate means with which to examine the issue fully, a conclusion supported by the present work is that for finite Reynolds numbers there are always four (axisymmetric) cells—two are encountered on each axial traverse away from the origin of the sphere. The extents of the inner cells appear to grow without bound as  $A/D \rightarrow 0$  for all finite Reynolds numbers: In the Stokes flow limit, only the inner cells remain.

A more realistic basis for assessment of mass transfer from particles or drops in oscillatory axisymmetric flows would involve simulations in which the sphere was free to move in response to drag forces, which are not difficult to

TABLE II. Peak drag coefficients for a sphere oscillating in quiescent fluid [see Fig. 13(b)]. Drag coefficients in steady flow are indicated by  $A/D = \infty$  (see Fig. 4).

$A/D \backslash Re$	1	2	5	10	20	50	100
0.05	80.4	55.9	37.3	29.2	23.9	19.6	17.6
0.1	60.9	40.2	25.1	18.7	14.6	11.3	9.80
0.2	48.5	30.5	17.8	12.6	9.36	6.82	5.67
0.5	38.5	22.9	12.3	8.17	5.70	3.82	2.99
1	34.0	19.5	9.96	6.36	4.29	2.75	2.08
2	31.1	17.3	8.57	5.35	3.53	2.20	1.60
5	28.9	15.8	7.68	4.71	3.04	1.83	1.30
$\infty$	27.3	14.9	7.14	4.31	2.72	1.58	1.09

TABLE III. Time-average Sherwood numbers for a sphere oscillating in quiescent fluid, or for a sphere in oscillatory flow [see Fig. 15(a)]. Sherwood numbers in steady flow are indicated by  $A/D = \infty$  (see Fig. 5).

$A/D \backslash Re$	1	2	5	10	20	50	100
0.05	2.02	2.02	2.01	2.01	2.01	2.13	2.48
0.1	2.02	2.02	2.01	2.00	1.99	2.11	2.60
0.2	2.02	2.02	2.01	1.99	1.95	2.04	2.61
0.5	2.03	2.03	2.02	1.99	1.93	2.06	3.00
1	2.04	2.06	2.07	2.07	2.06	2.48	4.06
2	2.06	2.10	2.18	2.25	2.35	3.19	4.94
5	2.11	2.18	2.36	2.54	2.80	3.77	5.11
$\infty$	2.31	2.52	2.96	3.47	4.20	5.57	6.96

arrange, but require introduction of another dimensionless parameter,  $\rho_s/\rho$ , i.e., the ratio of sphere to fluid density. Another issue that remains to be addressed is determination of the envelope of oscillation amplitudes and Reynolds numbers within which the flows retain their axisymmetry.

#### APPENDIX: TABULATED VALUES

Computed coefficients of drag and Sherwood numbers are presented in Tables II and III.

- <sup>1</sup>N. Riley, "On a sphere oscillating in a viscous fluid," *Q. J. Mech. Appl. Math.* **XIX**, 461 (1966).
- <sup>2</sup>E. J. Chang and M. R. Maxey, "Unsteady flow about a sphere at low to moderate Reynolds number. Part 1. Oscillatory motion," *J. Fluid Mech.* **277**, 347 (1994).
- <sup>3</sup>T. A. Johnson and V. C. Patel, "Flow past a sphere up to a Reynolds number of 300," *J. Fluid Mech.* **378**, 19 (1999).
- <sup>4</sup>A. G. Tomboulides and S. A. Orszag, "Numerical investigation of transitional and weak turbulent flow past a sphere," *J. Fluid Mech.* **416**, 45 (2000).
- <sup>5</sup>B. Ghidersa and J. Dusek, "Breaking of axisymmetry and onset of unsteadiness in the wake of a sphere," *J. Fluid Mech.* **423**, 33 (2000).
- <sup>6</sup>R. Mei, "Flow due to an oscillating sphere and an expression for unsteady drag on the sphere at finite Reynolds number," *J. Fluid Mech.* **270**, 133 (1994).
- <sup>7</sup>M. C. Thompson, T. Lewecke, and M. Provansal, "Kinematics and dynamics of sphere wake transition," *J. Fluids Struct.* **15**, 575 (2001).
- <sup>8</sup>F. Odar and W. S. Hamilton, "Forces on a sphere accelerating in a viscous fluid," *J. Fluid Mech.* **18**, 302 (1963).
- <sup>9</sup>H. Kramers, "Heat transfer from spheres to flowing media," *Physica (Amsterdam)* **XII**, 61 (1946).
- <sup>10</sup>H. Brenner, "Forced convection heat and mass transfer at small Peclet numbers from a particle of arbitrary shape," *Chem. Eng. Sci.* **18**, 109 (1963).
- <sup>11</sup>J. H. Masilyah and N. Epstein, "Numerical solution of heat and mass transfer from spheroids in steady axisymmetric flow," *Prog. Heat Mass Transfer* **6**, 613 (1972).
- <sup>12</sup>S. C. R. Dennis, J. D. A. Walker, and J. D. Hudson, "Heat transfer from a sphere at low Reynolds number," *J. Fluid Mech.* **60**, 273 (1973).
- <sup>13</sup>E. E. Michaelides and Z. Feng, "Heat transfer from a rigid sphere in a nonuniform flow and temperature field," *Int. J. Heat Mass Transf.* **43**, 2069 (1994).
- <sup>14</sup>Z. Feng and E. E. Michaelides, "Unsteady heat transfer from a sphere at small Peclet numbers," *ASME J. Fluids Eng.* **118**, 96 (1996).
- <sup>15</sup>Z. Feng and E. E. Michaelides, "A numerical study on the transient heat transfer from a sphere at high Reynolds and Peclet numbers," *Int. J. Heat Mass Transf.* **43**, 219 (2000).
- <sup>16</sup>S. L. Fraenkel, L. A. H. Nogueira, J. A. Carvalho, Jr., and F. S. Costa, "Heat transfer coefficients for drying in pulsating flows," *Int. Commun. Heat Mass Transfer* **25**, 471 (1998).
- <sup>17</sup>A. M. Al Taweel and J. Landau, "Mass transfer between solid spheres and oscillating fluids—a critical review," *Can. J. Chem. Eng.* **54**, 532 (1976).
- <sup>18</sup>C. K. Drummond and F. A. Lyman, "Mass transfer from a sphere in an oscillating flow with zero mean velocity," *Comput. Mech.* **6**, 315 (1990).
- <sup>19</sup>R. Clift, J. R. Grace, and M. E. Weber, *Bubbles, Drops, and Particles* (Academic, New York, 1978).
- <sup>20</sup>E. L. Cussler, *Diffusion: Mass Transfer in Fluid Systems*, 2nd ed. (Cambridge University Press, Cambridge, 1997).
- <sup>21</sup>G. E. Karniadakis, M. Israeli, and S. A. Orszag, "High-order splitting methods for the incompressible Navier–Stokes equations," *J. Comput. Phys.* **97**, 414 (1991).
- <sup>22</sup>E. M. Rønquist, "Optimal spectral element methods for the unsteady three-dimensional incompressible Navier–Stokes equations," Ph.D. thesis, Massachusetts Institute of Technology, 1988.
- <sup>23</sup>M. I. Gerritsma and T. N. Phillips, "Spectral element methods for axisymmetric Stokes problems," *J. Comput. Phys.* **164**, 81 (2000).
- <sup>24</sup>H. M. Blackburn and J. M. Lopez, "Modulated rotating waves in an enclosed swirling flow," *J. Fluid Mech.* **465**, 33 (2002).
- <sup>25</sup>A. B. Bassett, *A Treatise on Hydrodynamics, Vol II* (Deighton, Bell and Co., Cambridge, England, 1888). (Republished: Dover, New York, 1961.)
- <sup>26</sup>F. M. White, *Viscous Fluid Flow*, 2nd ed. (McGraw-Hill, New York, 1991).